Using X-ray Computed Tomography to Describe the Dynamics of Nitrous Oxide Emissions during Soil Drying

Eva Rabot, Marine Lacoste, Catherine Hénault, Isabelle Cousin

Vadose Zone Journal

Using X-ray computed tomography to describe the dynamics of nitrous oxide emissions during soil drying

Journal:	*Vadose Zone Journal*
Manuscript ID:	VZJ-2014-12-0177-ORA.R1
Manuscript Type:	Original Research Articles
Date Submitted by the Author:	10-Apr-2015
Complete List of Authors:	RABOT, Eva LACOSTE, Marine Henault, Catherine Cousin, Isabelle
Keywords:	soil, nitrous oxide, X-ray computed tomography, gas diffusivity, pore connectivity

Using X-ray computed tomography to describe the dynamics of nitrous oxide emissions during soil drying

E. Rabot[1,2], M. Lacoste[2], C. Hénault[2], I. Cousin[2,*]

[1] Laboratoire Léon Brillouin, UMR12, CEA Saclay, 91191 Gif-sur-Yvette Cedex, France

[2] INRA, UR0272, UR Science du Sol, F-45075 Orléans, France

* Corresponding author: isabelle.cousin@orleans.inra.fr

Impact statement

We proposed a methodology to image the water dynamics and the soil structure of a soil sample with X-ray computed tomography, while controlling the hydric state and monitoring N_2O fluxes. Relevant information about N_2O transport could be extracted from the images.

Abstract

Water in soil is known to be a key factor for controlling nitrous oxide (N_2O) emissions, because N_2O is mainly produced by denitrification in anoxic environments. In this study, we proposed a methodology to image the water and soil structure of a soil sample with X-ray computed tomography, while controlling the hydric state and monitoring N_2O fluxes. We used a multistep outflow system to apply two wetting-drying cycles to an undisturbed soil. The soil core was scanned with coarse-resolution X-ray computed tomography, one time during wetting and several times during drying, to measure quantitative and qualitative indicators of the pore network. Nitrous oxide emissions were higher during the first (C1) than during the second (C2) wetting-drying cycle, both for the wetting and the drying phases. Fluxes increased quickly after the beginning of the drying phase to reach a peak after 5 h. Differences in the intensity of N_2O emissions between the two cycles were attributed to differences in the water saturation, air-phase connectivity, and relative gas diffusion coefficient, which led to more or less N_2O production, consumption, and entrapment in soil. The speed of the N_2O emissions at the beginning of the drying phase depended on the rate of increase of the air-filled pore volume and connectivity, and was especially well described by the estimated relative gas diffusion coefficient. Parameters of the soil structure were not able to explain completely the intensity of N_2O emissions during drying: N_2O production and consumption factors were also involved.

Abbreviations: C1: first wetting-drying cycle; C2: second wetting-drying cycle; WFPS: water filled pore space.

1 Introduction

Nitrous oxide (N_2O) concentration in the atmosphere is constantly increasing (Khalil et al., 2002). With a global warming potential 300 times higher than that of carbon dioxide over a 100-year time scale (World Meteorological Organization, 2007), N_2O is the gas with the third largest contribution to global warming (Ciais et al., 2013). Nitrous oxide plays also an important role in the stratospheric ozone depletion (Ravishankara et al., 2009). Soils are a major source of N_2O, accounting for 60% of natural sources (soils under natural vegetation) and 60% of anthropogenic sources (soils used for agriculture; Ciais et al., 2013). Nitrous oxide is produced during the natural microbial reactions of nitrification and denitrification, two reactions which are controlled by the status of aerobiosis in soils. Since the water saturation of soils modifies the ratio between water-filled and air-filled pore space, the water-filled pore space (WFPS) is often used as an indicator of N_2O emissions (Butterbach-Bahl et al., 2013; Robertson, 1989). In particular, wetting and drying cycles are known to affect N_2O emissions (Guo et al., 2014; Muhr et al., 2008). Peaks of N_2O emissions have often been observed both in the field and in laboratory experiments after the rewetting of a soil (Groffman and Tiedje, 1988; Sanchez-Martin et al., 2010; Sexstone et al., 1985).

Following the model proposed by Smith (1980), N_2O production can occur inside anoxic aggregates and then diffuse to the soil surface through inter-aggregate pores. Thus, delays between microbial production and the moment when N_2O can be measured at the soil surface have been demonstrated (Clough et al., 1998; McCarty et al., 1999; Rabot et al., 2014; Weier et al., 1993; Wollersheim et al., 1987). Delays in N_2O emissions are partly linked to gas entrapment and the associated dissolution of N_2O in the water phase (Clough et al., 2005). We hypothesize here that introducing dynamic indicators of the soil structure could enhance our

55 understanding of the dynamic nature of N_2O emissions during wetting and drying cycles, by a
56 better description of N_2O transport. Indeed, since soil structure controls the water and gas
57 dynamics in soils, and thus the aerobic microbial activity, soil structure is supposed to be of
58 great importance for N_2O emissions (Ball, 2013).

59 Both the soil water and soil structure can be studied by X-ray computed tomography. X-ray
60 computed tomography is rapid, non-destructive, and allows successive scans over time while
61 measuring other dynamic parameters, such as N_2O fluxes. It provides 3-D images, used to
62 perform spatial analysis of the soil sample. In soil science, X-ray computed tomography is a
63 common tool, used for example to study the effect of agricultural practices (Deurer et al.,
64 2009; Schjønning et al., 2013; Schlüter et al., 2011), the water dynamics (Kasteel et al., 2000;
65 Sammartino et al., 2012; Wildenschild et al., 2005), or the gas dynamics (Deurer et al., 2009;
66 Katuwal et al., 2014; Naveed et al., 2013). Katuwal et al. (2014) demonstrated the interest of
67 coarse-resolution X-ray scanners to study gas transport functioning in macropores. This
68 methodology can be applied to N_2O emissions. Only few studies used imaging techniques to
69 study greenhouse gas emissions (e.g., Mangalassery et al., 2014; Mangalassery et al., 2013),
70 and to our knowledge, none of them monitored greenhouse gases while acquiring images of
71 the soil structure.

72 In this study, we proposed a methodology to image the water and soil structure of a soil
73 sample with coarse-resolution X-ray computed tomography, while controlling the hydric state
74 and monitoring N_2O fluxes. We aimed at demonstrating which relevant information can be
75 extracted from the images to allow a better understanding of N_2O emissions. We illustrated
76 this methodology by subjecting a soil sample to two wetting and drying cycles.

2 Material and methods

2.1 Soil sampling, physical and chemical characterization

The study site was chosen for the high N_2O emissions previously recorded in the field (Gu et al., 2011), at the same location as the study of Rabot et al. (2014). The site is an agricultural field cultivated with rape (*Brassica napus* L.), located near Chartres, in the northwest of France (48.376° N lat, 1.196° E long). The soil is classified as Glossic Retisol (WRB, 2014), with a clay content of 13.7%, a silt content of 82.0%, and a sand content of 4.3% (Rabot et al., 2014). A soil core was collected in June 2013 in a PVC cylinder (13.2-cm inner diameter by 7-cm height) from the surface horizon (1–8 cm). Bulk soil was also sampled in the surface horizon for physical and chemical analyses. Soil organic carbon was measured by sulfochromic oxidation, and total nitrogen was measured by the Dumas method. The soil nitrate content was determined by colorimetric analysis after the extraction from an 8-g soil sample using 0.5 M K_2SO_4. Soil pH was determined in a 1:2.5 soil/water volume ratio on samples sieved at < 2 mm. At the sampling time, the soil organic carbon was 9.5 g kg^{-1}, the total nitrogen content was 0.91 g kg^{-1}, the nitrate content was 51.3 mg NO_3^-–N kg^{-1}, and the soil pH was 5.6. The porosity of the soil sample was 0.46 cm^3 cm^{-3} and the volumetric water content was 37.7% (equivalent to 81.9% WFPS). The sample was conditioned in a plastic bag and stored field moist during two weeks at 5°C to minimize microbial activity. Before the start of the experiment, the soil core was trimmed on each end and maintained at 20°C for 24 h.

2.2 Experimental setup

The experiment consisted in controlling the hydric status of the soil sample with a multistep outflow system (Weihermüller et al., 2009): the soil cylinder was connected to a water-tank to control its wetting according to the Mariotte bottle principle, and connected to a vacuum

pump and a sampling bottle to control its drying (Fig. 1). Hydraulic continuity was ensured with a porous ceramic plate (1-bar air-entry value, 8.6×10^{-8} m s^{-1} saturated hydraulic conductivity, Soilmoisture Equipment Corp.) placed at the bottom of the soil cylinder and previously saturated with water. The soil cylinder-ceramic plate system was sealed with silicon to avoid water or gas leaks. Both the water content and water potential were continuously monitored during the experiment, with a balance (0.1 g precision) and two microtensiometers (porous ceramic cup, 20-mm length, 2.2-mm diam., 150-kPa air-entry value) inserted at 2 and 4 cm from the cylinder surface at the end of the wetting phase. Data were recorded every 10 min with a datalogger (CR1000, Campbell Scientific).

Two wetting-drying cycles (hereafter referred to as the C1 and C2 cycles) were applied to the soil cylinder. The initial water content for C1 was the water content at sampling. The sample was first saturated for 3 d by raising the water level to the soil surface in one step, and then a –100 hPa pressure was applied at the bottom of the soil core in one step, and maintained for about 7 h (C1 cycle). A zero hPa pressure was then applied for 3 d, followed by a –100 hPa pressure for about 7 h (C2 cycle). Indeed, Rabot et al. (2014) demonstrated that N_2O peaks can be created during the drying phase, at a matric potential of approximately –50 hPa. We chose thus to apply a pressure lower than this value of –50 hPa. The speed of the matric potential decrease was much higher that under natural conditions, and could affect the water transport and hydraulic continuity. We used a KNO_3 solution as the wetting fluid, to ensure that nitrate was not a limiting factor for N_2O emissions during the wetting phase, and to isolate the effects of nitrate concentration and soil moisture on the N_2O emissions. Hénault and Germon (2000) showed that the response of N_2O emissions to the nitrate concentration could be described by a Michaelis-Menten function. We used a nitrate concentration at the plateau of this function (4.1 mM N). The nitrate solution was prepared with de-aired water to prevent air bubble formation during the experiment.

Nitrous oxide emissions were monitored by infrared correlation spectroscopy (N_2O Analyzer model 46i, Thermo Scientific) using a 4-L volume closed-chamber. The emissions were measured for 20-min periods, and the concentration value was recorded every minute. Given the linear increase of the N_2O concentration in the closed-chamber, N_2O fluxes were calculated linearly from the observed change in concentration during the first 10 min after the chamber was closed. Only one N_2O flux measurement was done during wetting, at the end of each wetting phase for each cycle, and seven (respectively eight) flux measurements were recorded during the drying phase for the C1 (respectively C2) cycle. Moreover, gases inside the chamber were sampled in evacuated vials at the end of the wetting phase and at the middle of the drying phase (3.5 h after the beginning of the drying phase), and CO_2 concentration was determined by gas chromatography (μGC Gas Analyzer T-3000, SRA Instruments). For a single CO_2 flux measurement, the atmosphere of the closed-chamber was sampled three times during 20-min periods. Given the linear increase of the CO_2 concentration, the flux was then calculated linearly. The chamber was removed before each measurement to restore the atmosphere to ambient concentrations of gases. The sample was kept inside the scanner during the two wetting-drying cycles. The temperature inside the scanner room was monitored and ranged between 22.5 and 25.5°C throughout the experiment.

2.3 Computed tomography and image analyses

The soil sample was placed in the scanner in its sampling direction. The soil sample was scanned one time at the end of the wetting phase, and the vacuum pump was then activated to begin the soil drying. We then scanned the sample seven times for C1, and nine times for C2 during the drying phase, alternating with N_2O flux measurements. Two scans have been added at C2 compared to C1 to refine the results just after the beginning of the drying phase. We used a medical X-ray tomograph (Siemens Somatom Definition AS) operating at an energy

level of 200 kV and a current of 140 mA. The voxel size was 316×316×100 µm. The scanning duration was 15 seconds. In the following, intensities are expressed in Hounsfield units (HU).

Most of the image processing was realized with the ImageJ software (Rasband, 1997-2014). Due to the chamber manipulation during the experiment and displacement of the sample between scans, image registration was first done to ensure spatial consistency between the different images with the Align3 TP plugin (Parker, 2012). We cropped the images to exclude non-soil areas, and we rescaled the images to get isotropic voxels of 316 µm. The noise was reduced by using a bilateral filter, and edges were enhanced with an unsharp mask (Schlüter et al., 2014). The air phase and the water phase were both separated from the soil matrix and gravels by using the watershed segmentation method. This method has previously been successfully used to segment images of soils (Schlüter et al., 2014). A majority filter with a 3×3×3 kernel was applied to remove very small air-filled and water-filled pores which can be seen as noise. We finally removed manually the signal of the two tensiometers. The procedure used to segment the air phase and the water phase gave satisfactory results (Fig. 2). Visualization of the air-filled and water-filled pore network was done with the ImageJ plugin 3-D Viewer (Schmid et al., 2010).

The volume of air-filled and water-filled macropores was estimated with the BoneJ plugin (Doube et al., 2010), and the Euler number was calculated considering 26-connectivity with the C library QuantIm v.4 (Vogel, 2008), on the segmented images. The Euler number characterizes the connectivity of the air-filled pore space (Vogel et al., 2010). When the Euler number is positive, the pore network is classified as unconnected, whereas it is connected when the Euler number is negative. The volume of air-filled macropores and Euler number were calculated on the total air-filled pores identified, and the air-filled pores connected to the soil surface only, to evaluate the pore network contributing to N_2O emissions. We estimated the relative gas diffusion coefficients D_S/D_0 from the segmented air-filled pore space with

QuantIm v.4 (Vogel, 2008), as already done by Deurer et al. (2009) and Vogel et al. (2002). The gas diffusion was modeled by using the Fick's law of diffusion in 3-D, solved by explicit finite differences. Throughout the simulation, the gas concentration at the bottom of the soil sample was fixed at a constant value, and the gas concentration at the top was set to zero. We calculated D_S/D_0 on subsamples of increasing thickness from the soil surface (adding 10 pixels at the bottom of the given subsample).

3 Results

3.1 Soil water content and soil water potential evolution

During the drying phase, the WFPS measured with the MSO system ranged between 85% and 79% at C1, and between 83% and 79% at C2. The soil matric potential was above 0 cm for the two wetting cycles for the –4 cm depth tensiometer, whereas it was slightly under 0 cm for the –2 cm depth tensiometer at C2 (Fig. 3). Saturation was thus slightly lower during C2. The matric potential showed a plateau at the C2 wetting phase, reached in approximately 4.5 h after the beginning of the C2 wetting phase. During the drying phase, the matric potential decreased linearly, immediately after activating the vacuum pump, to reach –56 cm water column at C1 and –67 cm water column at C2. The decrease of the matric potential was slightly faster at C2 than at C1 (mean decrease of –8.8 cm h^{-1} at C1, and –9.5 cm h^{-1} at C2).

3.2 Dynamics of the N_2O and CO_2 fluxes

Emissions were lower during C2 than during C1, both for the wetting and the drying phases, with the maximum N_2O flux being 55.1 mg N m^{-2} d^{-1} at C1, and 19.1 mg N m^{-2} d^{-1} at C2 (Fig. 3). Nitrous oxide fluxes were measured to be 9.4 and 0.1 mg N m^{-2} d^{-1} at the end of the C1 and C2 wetting phase, respectively. In comparison, they ranged between 0 and 2.6 mg N m^{-2} d^{-1} in the field measurements of Gu et al. (2011) on the same study site. Nitrous oxide

198 fluxes increased quickly during the drying phase to reach a peak approximately 5.5 h after the
199 beginning of the soil drying at C1, and 4.5 h at C2. Peaks occurred at a mean matric potential
200 of –41.1 cm water column at C1, and –44.7 cm at C2, and at a WFPS of 80.2% at C1 and
201 80.5% at C2. The increase in the N_2O fluxes was faster for C1 than for C2. The first flux
202 measurement of C1 was especially high (38.2 mg N m^{-2} d^{-1}) compared to the following
203 measurements. At C2, the fluxes measured at the beginning of the drying phase increased
204 more slowly, with fluxes between 3.3 and 3.9 mg N m^{-2} d^{-1} for the three first measurements.

205 Carbon dioxide fluxes were higher at C2 than at C1 at the end of the wetting phase (50.4 mg
206 CO_2 m^{-2} d^{-1} at C1, and 164.1 mg CO_2 m^{-2} d^{-1} at C2). An opposite trend was observed during
207 the drying phase: CO_2 fluxes were higher at C1 than at C2 (108.3 mg CO_2 m^{-2} d^{-1} at C1, and
208 76.1 mg CO_2 m^{-2} d^{-1} at C2). Soil pH at the end of the two wetting-drying cycles was 5.9.

209 **3.3 Characterization of the pore network**

210 Four components could be identified, both visually and in the histograms of each image: air
211 phase, water phase, soil matrix, and gravels (Fig. 4 and 5). We define the soil matrix as the
212 solid phase and pores with a size lower than the image resolution. Histograms appeared to be
213 unimodal, with the mode corresponding to the soil matrix, because the air-filled and water-
214 filled porosities represented only a small fraction of the soil sample volume (Fig. 4a and 4b).
215 A small peak near the pure air intensity value (–1024 HU) could be identified for the drying
216 phase, and a small peak near the pure water intensity value (0 HU) could be identified for the
217 wetting phase (Fig. 4c and 4d). Less water voxels and more air voxels were identified at C2
218 than at C1 during the wetting phase, showing that the water saturation was lower at C2 (Fig.
219 4c and 4d).

220 A 3-D rendering of the air phase and water phase distributions at the end of the wetting phase
221 and at the end of the drying phase for C1 and C2 is given in Fig. 5. Cylindrical pores,

222 probably earthworm burrows and root channels (of which one major root channel of
223 approximately 9 mm diameter), as well as smaller pores attributed to inter-aggregate voids are
224 visible. As expected, air-filled pores appeared to be more numerous at the end of the drying
225 phase than at the end of the wetting phase. A high volume of pore remained not saturated
226 during the experiment.

227 Most of the indicators calculated from the segmented images were highly correlated, except
228 the Euler number and D_S/D_0 (Table 1). Indeed, largest pores highly contributed to the
229 porosity, but relatively little to Euler number (Vogel et al., 2002), and D_S/D_0 includes
230 additional information about the tortuosity. The air-filled porosity identified ranged between
231 0.029 and 0.035 $cm^3\ cm^{-3}$ at C1, and between 0.023 and 0.035 $cm^3\ cm^{-3}$ at C2. In the driest
232 scan of C2, where the maximum air-filled pore volume has been identified, this air-filled
233 porosity is equivalent to 16% of the real air-filled porosity at a pressure of –100 hPa, or 7.5%
234 of the total porosity (0.46 $cm^3\ cm^{-3}$). For the total core volume, time-evolution of the air-
235 filled pore volume showed a rapid rise from the beginning to 1 h after the soil drying, and
236 then the system entered a state of equilibrium (Fig. 6a). C1 and C2 followed the same trend,
237 but the air-filled pore volume was significantly higher at C2 than at C1 at the end of the
238 wetting phase, and slightly higher at C2 than at C1 during the drying phase. The volume of
239 water-filled pores decreased quickly in the first hour of soil drying, and remained lower at C2
240 than at C1 during the whole experiment (Fig. 6a). The evolution of the air-filled pores
241 connected to the soil surface showed the same trend as for the total core volume, except that
242 no more difference can be seen between C1 and C2 after 2 h of soil drying (Fig. 6c).

243 For the total air-filled pore volume identified, the Euler number ranged between 1319 and
244 1849 at C1, and between 1405 and 1713 at C2 (Fig. 6b). Thus, the Euler number was positive
245 during the whole experiment, meaning that the air-filled pore network was unconnected at the
246 resolution of the images. The Euler number was lower at C2 than at C1 during the wetting

247 phase, and higher at C2 than at C1 during the drying phase. The air-filled pore connectivity
248 was thus better at C1 during the drying phase. The value of the Euler number tended to
249 decrease with soil drying. For the air-filled pores connected to the soil surface only, the Euler
250 number ranged between −52.5 and 17 at C1, and between −57 and 1 at C2 (Fig. 6d). A
251 transition between an unconnected and a connected pore network occurred in the first hour of
252 soil drying: the Euler number was positive at the end of the wetting phase, and negative
253 during the drying phase. The inherent connectivity improved then as the soil dried. The Euler
254 number was higher at C1 than at C2 during the whole experiment. One major pore cluster,
255 representing 98% of the air-filled pore volume connected to the soil surface at the end of the
256 two drying phases, was responsible for the negative value of the Euler number. The other
257 pores were smaller and had a less complicated morphology.

258 Simulated relative gas diffusion coefficients were null for subsamples thicker than
259 approximately 3 cm at C1, and 4 cm at C2, because deepest pores were poorly connected to
260 the soil surface. Thus, only the upper part of the soil sample could participate to the fast N_2O
261 transport to the soil surface in the gaseous phase. The evolution with time of the gas diffusion
262 coefficient of a 3-cm-thick subsample is given in Fig. 7. Absolute values of D_S/D_0 ranged
263 between 0.000 and 0.009 at C1, and between 0.003 and 0.005 at C2. They were higher at C2
264 than at C1, except for the first measurement of the C1 drying phase. Relative gas diffusion
265 coefficients increased quickly after the beginning of the soil drying at C1, and then showed
266 lower values. This peak at C1 was concomitant with a fast increase of the N_2O flux. The
267 increase with soil drying was slower at C2 than at C1. Trends were similar for the estimation
268 of D_S/D_0 on thinner subsamples (data not shown).

4 Discussion

4.1 The use of X-ray computed tomography for greenhouse gas emission studies

The experiment of the present study appeared as the first report of coupling between soil imaging, greenhouse gas flux measurements, and hydric control measured on the same sample. The use of X-ray computed tomography allowed identifying spatially the water and gas phases in the macropores, and thus determining the air-filled pore volume of these macropores at successive moments during the soil drying. At the scanner resolution, only 16% of the real air-filled porosity was identified, and the rest remained unresolved. Indeed, we used a large sample, with a size typical of that used to determine soil hydraulic properties, to approach the representative elementary volume of the soil. The pixel size was thus coarse, approximately 300 µm. With such a resolution, only macropores are unequivocally recognized, i.e., pores > 300 µm with the nomenclature of Jarvis (2007). According to Young-Laplace law (assuming 0° degree contact angle, interfacial tension for air-water and spherical interfaces), these macropores are expected to drain at a water potential of –10 cm.

Identifying a higher range of pore sizes would have been informative since macropores participate to N_2O transport, whereas N_2O production rather occurs in fine pores of the matrix domain (Heincke and Kaupenjohann, 1999). However, such a coarse resolution has successfully been used in previous studies to link soil structure and gas diffusion. By using X-ray computed tomography at a resolution of approximately 500 µm, Katuwal et al. (2014) observed a high positive correlation between air permeability and the air-filled macroporosity identified in their images. Deurer et al. (2009) explained a major part of the variability of the gas diffusion coefficients by the air-filled porosity and connectivity of pores > 300 µm identified with imaging. In the present study, despite the significant fraction of the unresolved pores which were air-filled at the end of the two drying cycles, coarse-resolution X-ray computed tomography can be used to infer N_2O transport functioning. We also succeeded in

identifying differences in the soil moisture between the two wetting-drying cycles. This difference was consistent with the other parameters recorded, i.e., matric potential and WFPS, and allowed inferring differences in anoxia level in the soil profile between C1 and C2. Relative, instead of absolute, comparisons between the two wetting-drying cycles could thus be performed.

4.2 Nitrous oxide emissions and pore connectivity

After 3 days of water saturation, soil drying down to –45 cm water column induced maximum N_2O fluxes. This result has been previously observed by Rabot et al. (2014). They hypothesized that the gas diffusion coefficient increased as the soil dried and allowed the release of the N_2O previously entrapped during the wetting phase in the pore space or in the soil solution. Nitrous oxide entrapment in soils at high WFPS has already been highlighted in laboratory experiments (Clough et al., 1998; McCarty et al., 1999; Weier et al., 1993). In this new study, supplementary information about the soil structure was obtained and we were able to measure an increase of the air-filled macropores connected to the soil surface as the soil dried. The air-filled pore network connected to the soil surface was described as well interconnected during the drying phase. Fast N_2O transport in the gaseous phase could occur from the soil upper part connected to the atmosphere during the drying phase, where some biological hotspots could be active (Ball et al., 2008; van der Weerden et al., 2012). The porous network was probably also connected by pores of a size lower than the one recorded by the X-ray scanner, which represent approximately 85% of the air-filled pore space at a pressure of –100 hPa. The observed increase of the air-filled pore volume connected to the soil surface, pore connectivity, and relative coefficient of gas diffusion with soil drying favors the hypothesis of Rabot et al. (2014), stating that entrapped N_2O was released during the drying phase.

By considering the whole pore volume, the pore network was classified as unconnected during the experiment. Firstly, given that the value of the Euler number depends on the size of the lower pore which can be resolved (Vogel et al., 2010), the soil sample may have been connected by unresolved air-filled pores. With a coarse-resolution scanner, we underestimate the connectivity of the soil sample. Secondly, the Euler number is a metrics highly affected by isolated voxels (Renard and Allard, 2013), like unconnected structural pores or thresholding artifacts, leading to highly positive values. Katuwal et al. (2014) observed that the Euler number was not a good measure of macropore connectivity to compare soil samples. Evolution of the Euler number for the whole identified pore volume is thus difficult to interpret, especially as a large fraction of the pore space remained unresolved. We favor the use of the Euler number for the pores connected to the soil surface, which, by construction, includes less isolated pores. Despite a high computational cost, the estimation of D_S/D_0 from the segmented pore network appeared to better describe N_2O transport, by showing an evolution similar to that of N_2O fluxes: a fast increase at C1 and a slow increase at C2. The relative gas diffusion coefficient provided comprehensive information, by taking into account the pore network connectivity and tortuosity, and was less affected by isolated voxels.

4.3 Intensity of nitrous oxide emissions

By comparing the two wetting and drying cycles, differences in the amount of N_2O emitted were observed. Emissions were lower at C2 than at C1 both during the wetting and the drying phases. A lower water content at C2 may have been responsible for the lower N_2O production during the C2 wetting phase. Moreover, the higher connectivity and relative gas diffusion coefficient at C2 during the wetting phase caused lower N_2O entrapment in soil, and could also explain the lower N_2O release during the C2 drying phase. Balaine et al. (2013) suggested that N_2O emissions were low for $D_S/D_0 < 0.006$ in their experiment on repacked soil samples at a hydric steady-state, because N_2O was entrapped in the soil and because the

reduction of N_2O into N_2 was high. The observations in our present study support these findings, as we estimated values of $D_S/D_0 < 0.006$ during the wetting phase, and we observed N_2O entrapment. Nitrous oxide reduction into N_2 is expected to occur two or three days after the water saturation of a soil sample (Letey et al., 1980). Nitrous oxide consumption probably occurred in the present study during the wetting phase, as WFPS > 90% favors this reaction (Ruser et al., 2006). Small differences in WFPS between the wetting phases of C1 and C2 could have caused differences in N_2O consumption. In the literature, reduced N_2O production after a second wetting and drying cycle has also been explained by the C and N dynamics in relation to the microbial dynamics activity (Fierer and Schimel, 2002; Mikha et al., 2005; Muhr et al., 2008). In our study, nitrate was supplied in excess during the wetting phase of each wetting-drying cycle, so nitrate was supposed not to be limiting at the beginning of each wetting-drying phase. On the contrary, the carbon dynamics can be implicated in the lower emissions at C2. A shortage of C after a first wetting-drying cycle may have consumed easily available C substrates (Fierer and Schimel, 2002), and/or less C substrates may have been exposed to microbial consumption at C2, by the physical disruption of soil aggregates during the wetting-drying cycles (Denef et al., 2001).

4.4 Timing of nitrous oxide emissions

In addition to the differences in terms of intensities of N_2O emissions between the two wetting and drying cycles, differences in the timing of the N_2O peaks were also observed. The matric potential appeared to be a good indicator of the timing of N_2O emissions, as already shown by Castellano et al. (2010), because the matric potential defines the diameter of the water-filled pores. We found that maximum N_2O fluxes were reached at approximately –45 cm water column, that is to say when pores with diameter > 66 µm were drained. This is consistent with the experiment of Castellano et al. (2010), who observed in their free drainage experiment that N_2O peaks occurred when pores with diameter > 80 µm were drained. In the experiment

of Balaine et al. (2013), N_2O peaks were observed when pores with diameter > 197 and > 57 µm were drained, in soils repacked at bulk densities 1.1 and 1.5 g cm^{-3}, respectively.

The timing can also be compared between the two wetting-drying cycles. In our study, N_2O fluxes were very high soon after the beginning of the C1 drying phase contrary to C2. Indeed, less N_2O may have been produced during the C2 wetting phase, leading to a lower gas concentration gradient between the soil surface and the atmosphere, and thus to a slower gas diffusion. Moreover, the lower rate of increase at C2 than at C1 of the air-filled pore volume, connectivity, and relative gas diffusion coefficient, at the beginning of the drying phase, could also explain the slower N_2O emissions at the beginning of the C2 drying phase. These variables were highly correlated, so only one of them could have been computed. The volume of air-filled pores and the Euler number of pores connected to the soil surface were easily calculated, but the relative gas diffusion coefficient appeared to be more efficient to describe the timing of N_2O emissions.

Conclusion

We hypothesized that introducing dynamic indicators of the soil structure could enhance our understanding of the dynamic nature of N_2O emissions by soils. The experiment performed in this study was intended to demonstrate the ability of a coupling between coarse-resolution X-ray computed tomography, hydric control and N_2O flux measurements, to better describe N_2O transport in soils. X-ray computed tomography is a rapid and non-destructive method, which allowed measuring an evolution of the air phase volume, pore connectivity, and estimating the relative gas diffusion coefficient during successive wetting-drying cycles on the same soil sample. Contrary to the use of other characterization techniques (e.g., measurements of the gas diffusion coefficient with the one-chamber method), the hydric status of the soil has not

been modified by supplementary wetting-drying cycles, and N_2O entrapment has not been disrupted.

We were able to measure an increase of the volume of the air phase connected to the soil surface, and an increase of the pore connectivity and gas diffusion coefficient as the soil dried. We used the Euler number as an indicator of the connectivity of the gas phase. Because this metrics is highly affected by isolated pores, we based our interpretations on the Euler number calculated for the pore space connected to the soil surface, rather than for the whole pore space identified with imaging. Nitrous oxide emissions were lower in terms of intensity and speed during the second drying cycle. Differences in the intensity of N_2O emissions were attributed to differences in the water saturation, air-phase connectivity, and relative gas diffusion coefficient, which led to more or less N_2O production, consumption, and entrapment in soil. The speed of the N_2O release at the beginning of the drying phase depended on the rate of increase of the air-filled pore volume, connectivity, and was especially well described by the relative gas diffusion coefficient. Parameters of the soil structure were not able to explain completely the intensity of N_2O emissions during drying, as N_2O production and consumption factors modified the N_2O concentration gradient between the soil and the atmosphere.

The soil structure can be seen as a factor of the N_2O flux intensity because the pore size controls N_2O production by providing a favorable microbial habitat (i.e., aerobic status, substrate availability, water potential), and because the pore tortuosity and connectivity to the soil surface controls N_2O emission. This study highlighted the need to find and measure dynamic indicators of the soil structure, to enhance our understanding of the dynamic nature of N_2O emissions by soils. The results presented here are an illustration based on one soil sample, but the methodology is widely applicable. Even if imaging with a coarse scanner

resolution provided valuable data, imaging techniques at a finer spatial resolution, able to identify pores with diameter of approximately 50 µm, would allow refining these results.

Acknowledgements

We are grateful to D. Colosse, P. Courtemanche, and G. Giot for their technical help in the experimental design and/or field sampling. We also thank S. Sammartino (INRA, UMR EMMAH) for help with the image analysis. CT-scan imaging was graciously performed by the CIRE platform (INRA Val de Loire, site de Tours, UMR PRC), and carbon and nitrogen analyses were graciously performed by the SAS Laboratoire. This work was supported by a Conseil Général du Loiret grant, by the Spatioflux program funded by the Région Centre, FEDER, INRA and BRGM, and by the Labex VOLTAIRE (ANR-10-LABX-100-01).

References

Balaine, N., T.J. Clough, M.H. Beare, S.M. Thomas, E.D. Meenken, and J.G. Ross. 2013. Changes in relative gas diffusivity explain soil nitrous oxide flux dynamics. Soil Sci. Soc. Am. J. 77:1496–1505.

Ball, B.C. 2013. Soil structure and greenhouse gas emissions: A synthesis of 20 years of experimentation. Eur. J. Soil Sci. 64:357–373.

Ball, B.C., I. Crichton, and G.W. Horgan. 2008. Dynamics of upward and downward N_2O and CO_2 fluxes in ploughed or no-tilled soils in relation to water-filled pore space, compaction and crop presence. Soil Tillage Res. 101:20–30.

Butterbach-Bahl, K., E.M. Baggs, M. Dannenmann, R. Kiese, and S. Zechmeister-Boltenstern. 2013. Nitrous oxide emissions from soils: How well do we understand the processes and their controls? Philos. Trans. R. Soc. B 368.

Castellano, M.J., J.P. Schmidt, J.P. Kaye, C. Walker, C.B. Graham, H. Lin, et al. 2010. Hydrological and biogeochemical controls on the timing and magnitude of nitrous oxide flux across an agricultural landscape. Glob. Change Biol. 16:2711–2720.

Ciais, P., C. Sabine, G. Bala, L. Bopp, V. Brovkin, J. Canadell, et al. 2013. Carbon and other biogeochemical cycles. In: Stocker, T.F., D. Qin, G.K. Plattner, M. Tignor, S.K. Allen, J. Boschung, et al., editors, Climate change 2013: The physical science basis. Contribution of working group I to the fifth assessment report of the intergovernmental panel on climate change. Cambridge University Press, Cambridge, United Kingdom and New York, NY, USA. p. 465–570.

Clough, T.J., S.C. Jarvis, E.R. Dixon, R.J. Stevens, R.J. Laughlin, and D.J. Hatch. 1998. Carbon induced subsoil denitrification of ^{15}N-labelled nitrate in 1 m deep soil columns. Soil Biol. Biochem. 31:31–41.

449 Clough, T.J., R.R. Sherlock, and D.E. Rolston. 2005. A review of the movement and fate of
450 N_2O in the subsoil. Nutr. Cycl. Agroecosyst. 72:3–11.

451 Denef, K., J. Six, H. Bossuyt, S.D. Frey, E.T. Elliott, R. Merckx, et al. 2001. Influence of dry-
452 wet cycles on the interrelationship between aggregate, particulate organic matter, and
453 microbial community dynamics. Soil Biol. Biochem. 33:1599–1611.

454 Deurer, M., D. Grinev, I. Young, B.E. Clothier, and K. Müller. 2009. The impact of soil
455 carbon management on soil macropore structure: A comparison of two apple orchard
456 systems in New Zealand. Eur. J. Soil Sci. 60:945–955.

457 Doube, M., M.M. Klosowski, I. Arganda-Carreras, F.P. Cordelières, R.P. Dougherty, J.S.
458 Jackson, et al. 2010. BoneJ: Free and extensible bone image analysis in ImageJ. Bone
459 47:1076–1079.

460 Fierer, N., and J.P. Schimel. 2002. Effects of drying-rewetting frequency on soil carbon and
461 nitrogen transformations. Soil Biol. Biochem. 34:777–787.

462 Groffman, P.M., and J.M. Tiedje. 1988. Denitrification hysteresis during wetting and drying
463 cycles in soil. Soil Sci. Soc. Am. J. 52:1626–1629.

464 Gu, J.X., B. Nicoullaud, P. Rochette, D.J. Pennock, C. Hénault, P. Cellier, et al. 2011. Effect
465 of topography on nitrous oxide emissions from winter wheat fields in Central France.
466 Environ. Pollut. 159:3149–3155.

467 Guo, X.B., C.F. Drury, X.M. Yang, W.D. Reynolds, and R.Q. Fan. 2014. The extent of soil
468 drying and rewetting affects nitrous oxide emissions, denitrification, and nitrogen
469 mineralization. Soil Sci. Soc. Am. J. 78:194–204.

470 Heincke, M., and M. Kaupenjohann. 1999. Effects of soil solution on the dynamics of N_2O
471 emissions: A review. Nutr. Cycl. Agroecosyst. 55:133–157.

Hénault, C., and J.C. Germon. 2000. NEMIS, a predictive model of denitrification on the field scale. Eur. J. Soil Sci. 51:257–270.

Jarvis, N.J. 2007. A review of non-equilibrium water flow and solute transport in soil macropores: Principles, controlling factors and consequences for water quality. Eur. J. Soil Sci. 58:523–546.

Kasteel, R., H.J. Vogel, and K. Roth. 2000. From local hydraulic properties to effective transport in soil. Eur. J. Soil Sci. 51:81–91.

Katuwal, S., T. Norgaard, P. Moldrup, M. Lamandé, D. Wildenschild, and L.W. de Jonge. 2015. Linking air and water transport in intact soils to macropore characteristics inferred from X-ray computed tomography. Geoderma 237–238:9–20.

Khalil, M.A.K., R.A. Rasmussen, and M.J. Shearer. 2002. Atmospheric nitrous oxide: Patterns of global change during recent decades and centuries. Chemosphere 47:807–821.

Letey, J., N. Valoras, A. Hadas, and D.D. Focht. 1980. Effect of air-filled porosity, nitrate concentration, and time on the ratio of N_2O/N_2 evolution during denitrification. J. Environ. Qual. 9:227–231.

Mangalassery, S., S. Sjögersten, D.L. Sparkes, C.J. Sturrock, J. Craigon, and S.J. Mooney. 2014. To what extent can zero tillage lead to a reduction in greenhouse gas emissions from temperate soils? Sci. Rep. 4, 4586.

Mangalassery, S., S. Sjögersten, D.L. Sparkes, C.J. Sturrock, and S.J. Mooney. 2013. The effect of soil aggregate size on pore structure and its consequence on emission of greenhouse gases. Soil Tillage Res. 132:39–46.

494 McCarty, G.W., D.R. Shelton, and A.M. Sadeghi. 1999. Influence of air porosity on
495 distribution of gases in soil under assay for denitrification. Biol. Fert. Soils 30:173–
496 178.

497 Mikha, M.M., C.W. Rice, and G.A. Milliken. 2005. Carbon and nitrogen mineralization as
498 affected by drying and wetting cycles. Soil Biol. Biochem. 37:339–347.

499 Muhr, J., S.D. Goldberg, W. Borken, and G. Gebauer. 2008. Repeated drying-rewetting cycles
500 and their effects on the emission of CO_2, N_2O, NO, and CH_4 in a forest soil. J. Plant
501 Nutr. Soil Sci. 171:719–728.

502 Naveed, M., S. Hamamoto, K. Kawamoto, T. Sakaki., M. Takahashi, T. Komatsu, et al. 2013.
503 Correlating gas transport parameters and X-ray computed tomography measurements
504 in porous media. Soil Sci. 178:60–68.

505 Parker, J.A. 2012. Stack Alignment (Align3_TP).
506 http://www.med.harvard.edu/jpnm/ij/plugins/Align3TP.html.

507 Rabot, E., C. Hénault, and I. Cousin. 2014. Temporal variability of nitrous oxide emissions by
508 soils as affected by hydric history. Soil Sci. Soc. Am. J. 78:434–444.

509 Rasband, W.S. 1997-2014. ImageJ. U.S. National Institutes of Health, Bethesda, Maryland,
510 USA, http://imagej.nih.gov/ij.

511 Ravishankara, A.R., J.S. Daniel, and R.W. Portmann. 2009. Nitrous oxide (N_2O): The
512 dominant ozone-depleting substance emitted in the 21st century. Science 326:123–125.

513 Renard, P., and D. Allard. 2013. Connectivity metrics for subsurface flow and transport. Adv.
514 Water Resour. 51:168–196.

515 Ruser, R., H. Flessa, R. Russow, G. Schmidt, F. Buegger, and J.C. Munch. 2006. Emission of
516 N_2O, N_2 and CO_2 from soil fertilized with nitrate: Effect of compaction, soil moisture
517 and rewetting. Soil Biol. Biochem. 38:263–274.

518 Robertson, G.P. 1989. Nitrification and denitrification in humid tropical ecosystems: Potential
519 controls on nitrogen retention. In: J. Proctor, editor, Mineral nutrients in tropical forest
520 and savanna ecosystems. Blackwell Science, Oxford, U.K. p. 55–69.

521 Sammartino, S., E. Michel, and Y. Capowiez. 2012. A novel method to visualize and
522 characterize preferential flow in undisturbed soil cores by using multislice helical CT.
523 Vadose Zone J. 11:86–98.

524 Sanchez-Martin, L., A. Sanz-Cobena, A. Meijide, M. Quemada, and A. Vallejo. 2010. The
525 importance of the fallow period for N_2O and CH_4 fluxes and nitrate leaching in a
526 Mediterranean irrigated agroecosystem. Eur. J. Soil Sci. 61:710–720.

527 Schjønning, P., M. Lamandé, F.E. Berisso, A. Simojoki, L. Alakukku, and R.R. Andreasen.
528 2013. Gas diffusion, non-darcy air permeability, and computed tomography images of
529 a clay subsoil affected by compaction. Soil Sci. Soc. Am. J. 77:1977–1990.

530 Schlüter, S., A. Sheppard, K. Brown, and D. Wildenschild. 2014. Image processing of
531 multiphase images obtained via X-ray microtomography: A review. Water Resour.
532 Res. 50:3615–3639.

533 Schlüter, S., U. Weller, and H.J. Vogel. 2011. Soil-structure development including seasonal
534 dynamics in a long-term fertilization experiment. J. Plant Nutr. Soil Sci. 174:395–403.

535 Schmid, B., J. Schindelin, A. Cardona, M. Longair, and M. Heisenberg. 2010. A high-level
536 3D visualization API for Java and ImageJ. BMC Bioinformatics 11.

537 Sexstone, A.J., T.B. Parkin, and J.M. Tiedje. 1985. Temporal response of soil denitrification
538 rates to rainfall and irrigation. Soil Sci. Soc. Am. J. 49:99–103.

539 Smith, K.A. 1980. A model of the extent of anaerobic zones in aggregated soils, and its
540 potential application to estimates of denitrification. J. Soil Sci. 31:263–277.

541 van der Weerden, T.J., F.M. Kelliher, and C.A.M. de Klein. 2012. Influence of pore size
542 distribution and soil water content on nitrous oxide emissions. Soil Res. 50:125–135.

543 Vogel, H.J. 2008. QuantIm: C/C++ library for scientific image processing. Helmholtz Center
544 for Environmental Research, Halle, Germany.

545 Vogel, H.J, I. Cousin, and K. Roth. 2002. Quantification of pore structure and gas diffusion as
546 function of scale. Eur. J. Soil Sci. 53:465–473.

547 Vogel, H.J., U. Weller, and S. Schlüter. 2010. Quantification of soil structure based on
548 Minkowski functions. Comput. Geosci. 36:1236–1245.

549 Weier, K.L., J.W. Doran, J.F. Power, and D.T. Walters. 1993. Denitrification and the
550 dinitrogen/nitrous oxide ratio as affected by soil water, available carbon, and nitrate.
551 Soil Sci. Soc. Am. J. 57:66–72.

552 Weihermüller, L., J.A. Huisman, A. Graf, M. Herbst, and J.M. Sequaris. 2009. Multistep
553 outflow experiments to determine soil physical and carbon dioxide production
554 parameters. Vadose Zone J. 8:772–782.

555 Wildenschild, D., J.W. Hopmans, M.L. Rivers, and A.J.R. Kent. 2005. Quantitative analysis
556 of flow processes in a sand using synchrotron-based X-ray microtomography. Vadose
557 Zone J. 4:112–126.

558 Wollersheim, R., G. Trolldenier, and H. Beringer. 1987. Effect of bulk density and soil water
559 tension on denitrification in the rhizosphere of spring wheat (Triticum vulgare). Biol.
560 Fert. Soils 5:181–187.

561 World Meteorological Organization. 2007. Scientific assessment of ozone depletion: 2006,
562 global ozone research and monitoring project. Global Ozone Res. Monit. Project Rep.
563 50. World Meteorol. Organ., Geneva

564 **Figure captions**

565 **Fig. 1.** Schematic overview of the multistep outflow system for hydric control and nitrous
566 oxide measurements. Intensity values corresponding to air and water are zoomed in (c) and
567 (d).

568 **Fig. 2.** Example of a gray scale slice with the segmented water and air, at the end of the
569 wetting phase and at the end of the drying phase.

570 **Fig. 3.** Evolution with time of the nitrous oxide fluxes and the matric potential measured by
571 the two tensiometers. Gray areas represent the drying phases, and white areas the wetting
572 phases. C1 is the first wetting-drying cycle, and C2 is the second wetting-drying cycle.

573 **Fig. 4.** Histograms of intensity values (16-bit), for (a) the first wetting-drying cycle, and (b)
574 the second wetting-drying cycle. Intensity values corresponding to air and water are zoomed
575 in (c) and (d).

576 **Fig. 5.** Three-dimensional distribution of the air phase (grey) and the water phase (blue) at the
577 end of the wetting phase and at the end of the drying phase for the two wetting-drying cycles.

578 **Fig. 6.** Evolution with time of (a) the air-filled and water-filled pore volume, and (b) the Euler
579 number of the total pore volume, (c) the air-filled pore volume, and (d) the Euler number of
580 the pores connected to the soil surface, for the first and second wetting-drying cycles. The
581 zero reference time is the beginning of the drying phase.

582 **Fig. 7.** Evolution with time of the relative gas diffusion coefficient of a 3-cm-thick subsample,
583 for the first and second wetting-drying cycles. The zero reference time is the beginning of the
584 drying phase.

585 **Tables**

586 **Table 1. Pearson correlation matrix of the indicators extracted from the segmented X-ray images.**

Variables	Euler number (T)	Euler number (S)	Air volume (T)	Air volume (S)	Water volume (T)	Gas diffusion coefficient (T)
Euler number (T)	1.00					
Euler number (S)	0.44	1.00				
Air volume (T)	–0.67	–0.91	1.00			
Air volume (S)	–0.72	–0.86	0.99	1.00		
Water volume (T)	0.65	0.77	–0.94	–0.95	1.00	
Gas diffusion coefficient (T)	0.01	–0.12	0.23	0.24	–0.41	1.00

T, calculated on the total air-filled pores identified; S, calculated on the air-filled pores connected to the soil surface.

587

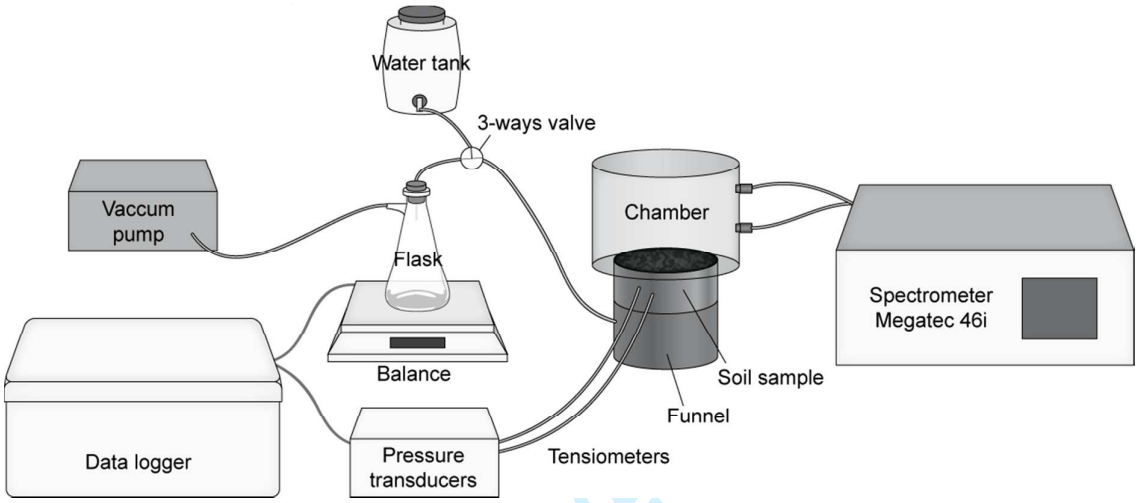

Fig. 1. Schematic overview of the multistep outflow system for hydric control and nitrous oxide measurements.

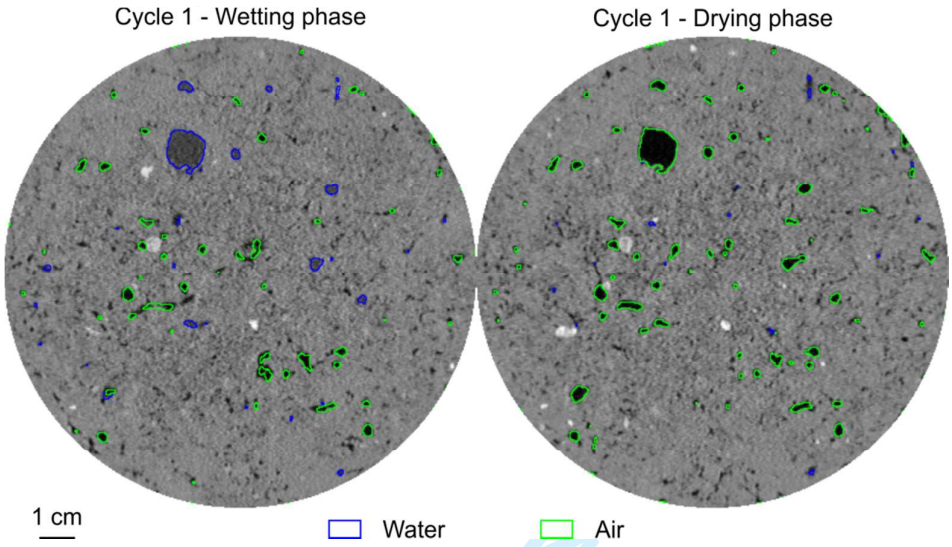

Fig. 2. Example of a gray scale slice with the segmented water and air, at the end of the wetting phase and at the end of the drying phase.

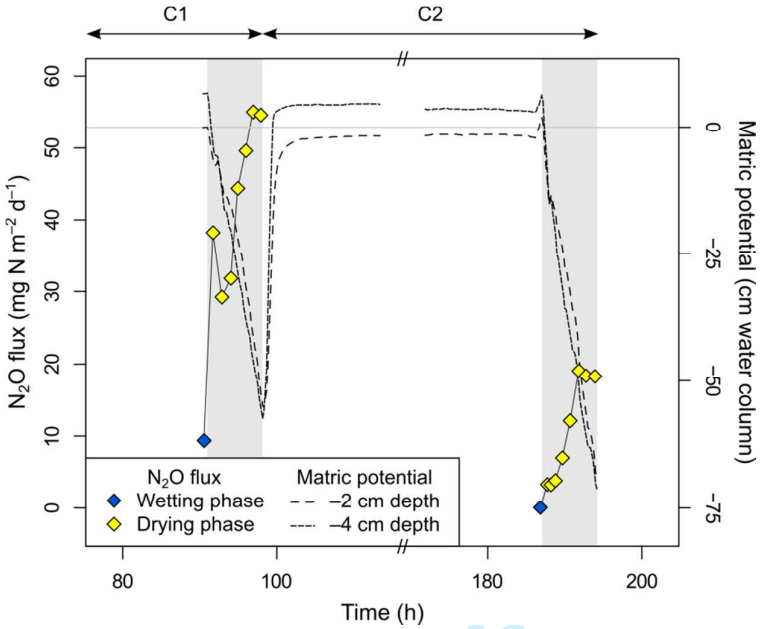

Fig. 3. Evolution with time of the nitrous oxide fluxes and the matric potential measured by the two tensiometers. Gray areas represent the drying phases, and white areas the wetting phases. C1 is the first wetting-drying cycle, and C2 is the second wetting-drying cycle.

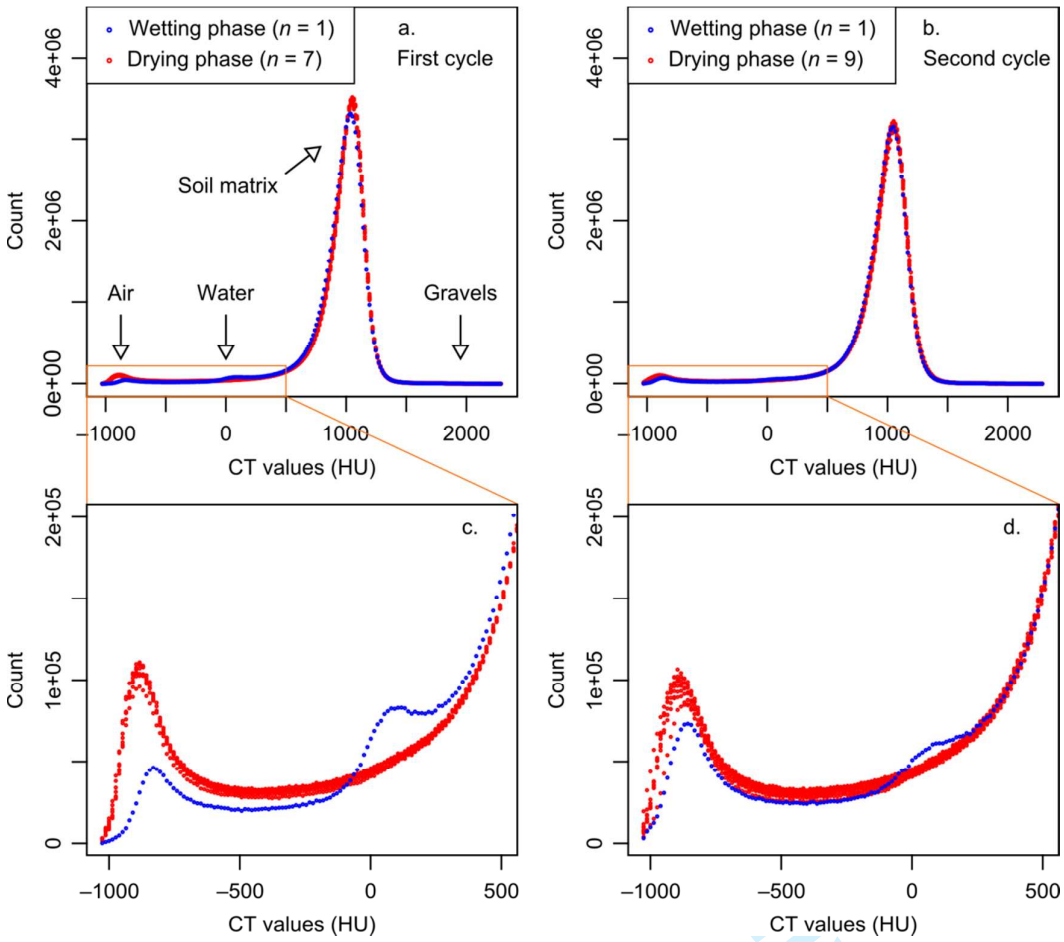

Fig. 4. Histograms of intensity values (16-bit), for (a) the first wetting-drying cycle, and (b) the second wetting-drying cycle. Intensity values corresponding to air and water are zoomed in (c) and (d).

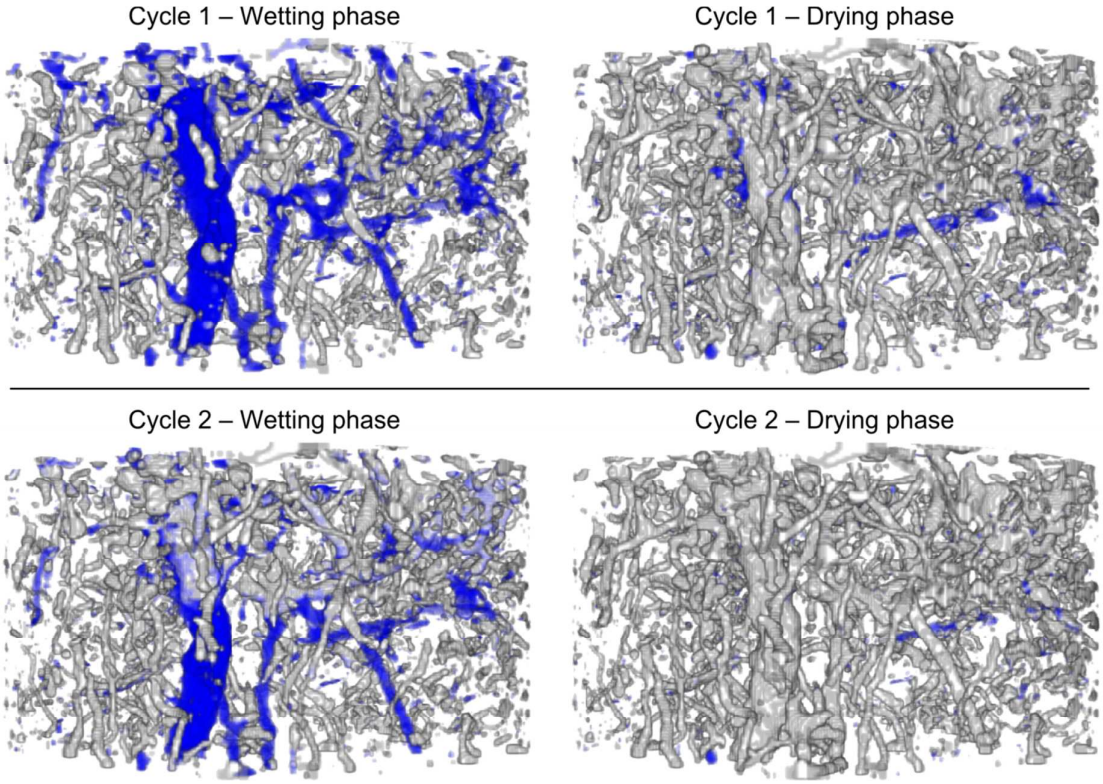

Fig. 5. Three-dimensional distribution of the air phase (grey) and the water phase (blue) at the end of the wetting phase and at the end of the drying phase for the two wetting-drying cycles.

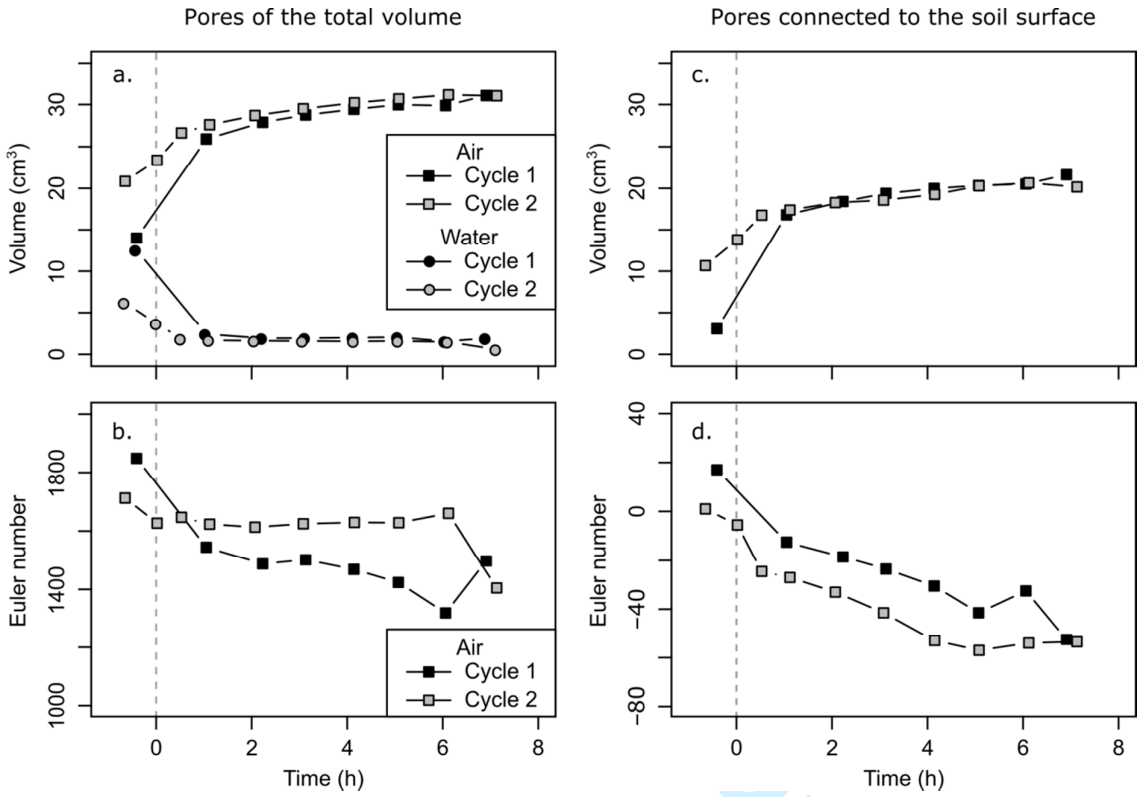

Fig. 6. Evolution with time of (a) the air-filled and water-filled pore volume, and (b) the Euler number of the total pore volume, (c) the air-filled pore volume, and (d) the Euler number of the pores connected to the soil surface, for the first and second wetting-drying cycles. The zero reference time is the beginning of the drying phase.

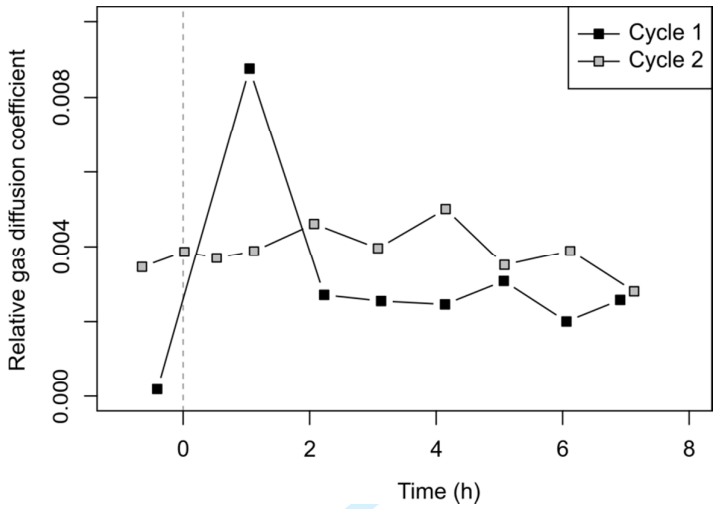

Fig. 7. Evolution with time of the relative gas diffusion coefficient of a 3-cm-thick subsample, for the first and second wetting-drying cycles. The zero reference time is the beginning of the drying phase.